LETTER

doi:10.1038/nature19787

Asthenosphere rheology inferred from observations of the 2012 Indian Ocean earthquake

Yan Hu[1,2], Roland Bürgmann[1], Paramesh Banerjee[3], Lujia Feng[3], Emma M. Hill[3], Takeo Ito[4], Takao Tabei[5] & Kelin Wang[6]

The concept of a weak asthenospheric layer underlying Earth's mobile tectonic plates is fundamental to our understanding of mantle convection and plate tectonics. However, little is known about the mechanical properties of the asthenosphere (the part of the upper mantle below the lithosphere) underlying the oceanic crust, which covers about 60 per cent of Earth's surface. Great earthquakes cause large coseismic crustal deformation in areas hundreds of kilometres away from and below the rupture area. Subsequent relaxation of the earthquake-induced stresses in the viscoelastic upper mantle leads to prolonged postseismic crustal deformation that may last several decades and can be recorded with geodetic methods[1–3]. The observed postseismic deformation helps us to understand the rheological properties of the upper mantle, but so far such measurements have been limited to continental-plate boundary zones. Here we consider the postseismic deformation of the very large (moment magnitude 8.6) 2012 Indian Ocean earthquake[4–6] to provide by far the most direct constraint on the structure of oceanic mantle rheology. In the first three years after the Indian Ocean earthquake, 37 continuous Global Navigation Satellite Systems stations in the region underwent horizontal northeastward displacements of up to 17 centimetres in a direction similar to that of the coseismic offsets. However, a few stations close to the rupture area that had experienced subsidence of up to about 4 centimetres during the earthquake rose by nearly 7 centimetres after the earthquake. Our three-dimensional viscoelastic finite-element models of the post-earthquake deformation show that a thin (30–200 kilometres), low-viscosity (having a steady-state Maxwell viscosity of (0.5–10) $\times$ 10^{18} pascal seconds) asthenospheric layer beneath the elastic oceanic lithosphere is required to produce the observed postseismic uplift.

We analysed the time series recorded by 47 continuous Global Navigation Satellite Systems (GNSS) stations, including 31 from the Sumatran Global Positioning System (GPS) Array (SuGAr), 11 from the International GNSS Service (IGS), 3 from the University of Memphis Andaman Island network, and 2 from the Aceh GPS Network for the Sumatran Fault System (AGNeSS). We selected 37 of these stations, those that show a coherent pattern of postseismic motions and do not have data gaps during the Indian Ocean earthquake (IOE) (Extended Data Fig. 1). The IOE produced static coseismic offsets of more than 20 cm at stations less than 500 km from the rupture area[7,8] and subsidence of up to about 4 cm (Fig. 1a). After removing the effects of previous earthquakes and the coseismic offsets of the IOE, as well as secular, annual and semi-annual trends (Extended Data Figs 2, 3)[9], we derived postseismic displacements of these stations in the first 3 years following the IOE. We find horizontal motion of up to about 17 cm in a landward direction similar to that of the coseismic displacements (Fig. 1b). The striking feature of the postseismic vertical displacement is that these middle-field stations within 300–500 km of the mainshock have risen by up to about 7 cm, reversing the coseismic subsidence, which is consistent with reported positive postseismic gravity changes in the same area[10].

On the basis of previous studies of subduction zone earthquakes in Sumatra[11,12] and other convergent margins[2,13,14], we constructed a viscoelastic finite-element model invoking the biviscous Burgers rheology[15] (Fig. 2) to study the postseismic deformation of the IOE. Transient Kelvin viscosity η_K is assumed to be one order of magnitude lower than the steady-state Maxwell viscosity η_M (the viscosity hereafter in this paper refers to the steady-state viscosity unless explicitly stated otherwise). Given the limited timespan of the GNSS data, we thus provide a lower-bound estimate of the steady-state viscosities.

The IOE involved a composite rupture of six strike-slip faults. Postseismic deformation at GNSS stations hundreds of kilometres from the rupture area is sensitive to the total moment of the earthquake, not to details of the slip distribution. Different coseismic fault slip models[6,7,16] predict different patterns of near-field postseismic displacements within 300 km of the mainshock but almost identical displacements at the GNSS stations (Extended Data Fig. 4). The coseismic fault slip distribution determined by Wei *et al.*[6] is used in this work.

We examine a number of first-order model scenarios to motivate our choice of primary model parameters, which we then evaluate in more detail. Assuming only one homogeneous viscoelastic layer below the elastic lithosphere, we need to use a low viscosity in the oceanic upper mantle of order 10^{19} Pa s to fit the observed horizontal GNSS data (Extended Data Fig. 5b). However, this test model results in postseismic subsidence that is inconsistent with the observed GNSS uplift. We find that models including a thin low-viscosity top layer of the oceanic asthenosphere can readily produce the observed uplift. Varying the lithospheric thickness by 20 km (Extended Data Fig. 6a, b) or imposing a smooth gradient in viscosity at the lithosphere–asthenosphere boundary (Extended Data Fig. 9c) produces negligible changes in the postseismic motions at GNSS stations. However, the effects of the subducting slab cannot be ignored (Extended Data Fig. 6c).

We assume the viscosity of the mantle wedge overlying the subducting Indo-Australian plate to be 3×10^{19} Pa s (ref. 13), but changing this value by one order of magnitude has little effect on predicted postseismic displacements at our GNSS stations. The postseismic surface deformation is controlled mainly by the rheological structure of the oceanic upper mantle (Extended Data Fig. 7). The rheological properties of the oceanic asthenosphere and upper mantle obtained in this work are better resolved at depths of less than 400 km because the IOE-induced stresses at greater depths are negligibly small (results not shown).

We use a grid-search method to determine preferred values of three model parameters from hundreds of models: the thickness (D_A) and viscosity (η_A) of the oceanic asthenosphere and the viscosity of the underlying oceanic upper mantle (η_O). We vary D_A, η_A and η_O within the ranges 10–300 km, 10^{17}–10^{20} Pa s and 10^{19}–10^{22} Pa s, respectively. To find the best-fit model parameters and their tradeoffs, we calculate

[1]Berkeley Seismological Laboratory and Department of Earth and Planetary Science, University of California Berkeley, Berkeley, California, USA. [2]Mengcheng National Geophysical Observatory, School of Earth and Space Sciences, University of Science and Technology of China, Hefei 230026, China. [3]Earth Observatory of Singapore, Asian School of the Environment, Nanyang Technological University, Singapore. [4]Graduate School of Environmental Studies, Nagoya University, Aichi 464-8601, Japan. [5]Department of Applied Science, Kochi University, Akebono-cho 2-5-1, Kochi 780-8520, Japan. [6]Pacific Geoscience Centre, Geological Survey of Canada, Natural Resources Canada, Sidney, British Columbia, Canada.

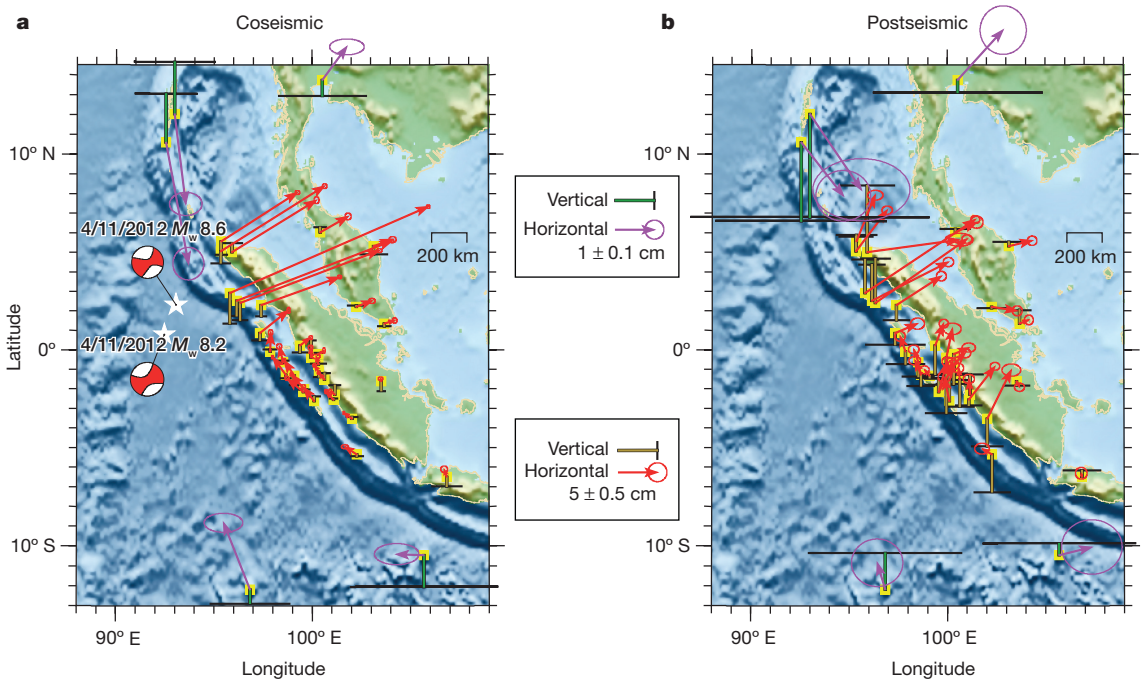

Figure 1 | Coseismic and cumulative three-year-postseismic GNSS observations of the IOE. Error bars represent 2σ (95%) confidence intervals. Yellow squares represent locations of the GNSS stations. **a**, Coseismic displacements of the IOE, estimated from static offsets of five days before and after the IOE (the IOE includes two events—the two beachballs—separated by about two hours). **b**, Cumulative three-year-postseismic displacements of the IOE in the Sunda reference frame (Supplementary Table 1). Red and magenta arrows represent horizontal GNSS displacements at different scales. Brown and green bars represent vertical GNSS displacements at different scales.

the χ^2 misfit of each test model prediction (equation (1) in Methods) to our GNSS displacements.

If we consider χ^2 only in the horizontal components (Fig. 3a), a test model fitting to the GNSS observations requires $D_A \geq 50$ km, η_A of the order of 10^{19} Pa s and $\eta_O \geq 10^{19}$ Pa s. The test model that best fits the horizontal GNSS motion does not predict the observed forearc uplift (Extended Data Fig. 9d). If we consider χ^2 only in the vertical component (Fig. 3b), a η_A value of the order of 10^{18} Pa s produces a good fit to the vertical GNSS displacements. The test model that best fits the vertical GNSS motion overestimates the horizontal components in the middle field (Extended Data Fig. 9e).

If we consider χ^2 in both the horizontal and vertical components (Fig. 3c), all three model parameters are constrained within a relatively narrow range. D_A, η_A and η_O are determined to be in the ranges 30–200 km, $(0.5–10) \times 10^{18}$ Pa s and $(0.5–100) \times 10^{20}$ Pa s, respectively. The lowest-χ^2 preferred model (PM) has $D_A = 80$ km, $\eta_A = 2 \times 10^{18}$ Pa s, and $\eta_O = 10^{20}$ Pa s (Extended Data Fig. 9f). The first-order mantle structure obtained in this work is consistent with results from a regional surface-wave tomography study[17] that indicates a low-velocity region centred at a depth of about 150 km.

There are important tradeoffs between model parameters, especially between the thickness and viscosity of the asthenospheric layer. If η_O is fixed at 10^{20} Pa s as in the PM, η_A scales with D_A because $\eta_A = aD_A^{1.5}$, where $a = 3.5 \times 10^{15}$ Pa s km$^{-1.5}$ (Fig. 4a), and D_A is in kilometres. This tradeoff is similar to the one found in models of isostatic rebound of continental regions that were covered by thick ice caps during the last ice age. Paulson *et al.*[18] analysed the postglacial rebound relying on long-wavelength (>700 km) Gravity Recovery And Climate Experiment (GRACE) satellite data in Canada and the sea-level history in Hudson Bay and reported a similar relationship, $\eta_A \propto D_A^3$.

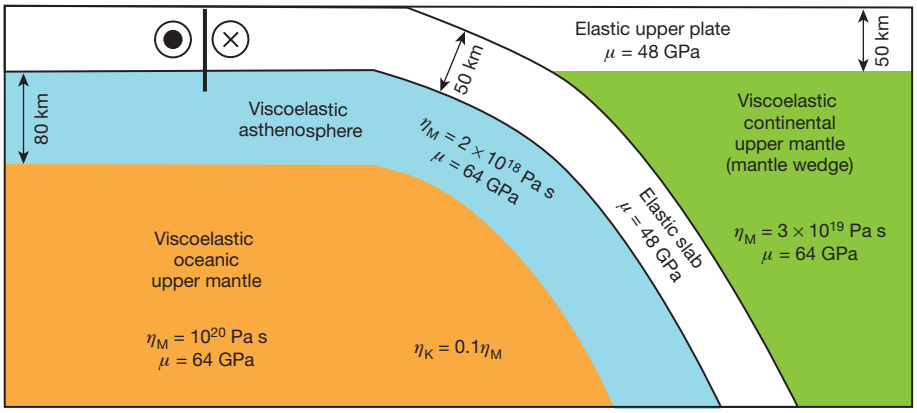

Figure 2 | Conceptual representation of the finite-element model. The model includes an elastic upper plate and elastic slab, viscoelastic continental upper mantle (mantle wedge), viscoelastic oceanic asthenosphere and viscoelastic oceanic upper mantle. The rock properties of each structural unit are given: μ, η_M and η_K represent the shear modulus, steady-state Maxwell and transient Kelvin viscosities, respectively. $\eta_K = 0.1\eta_M$. The thick black line illustrates the strike–slip fault of the IOE.

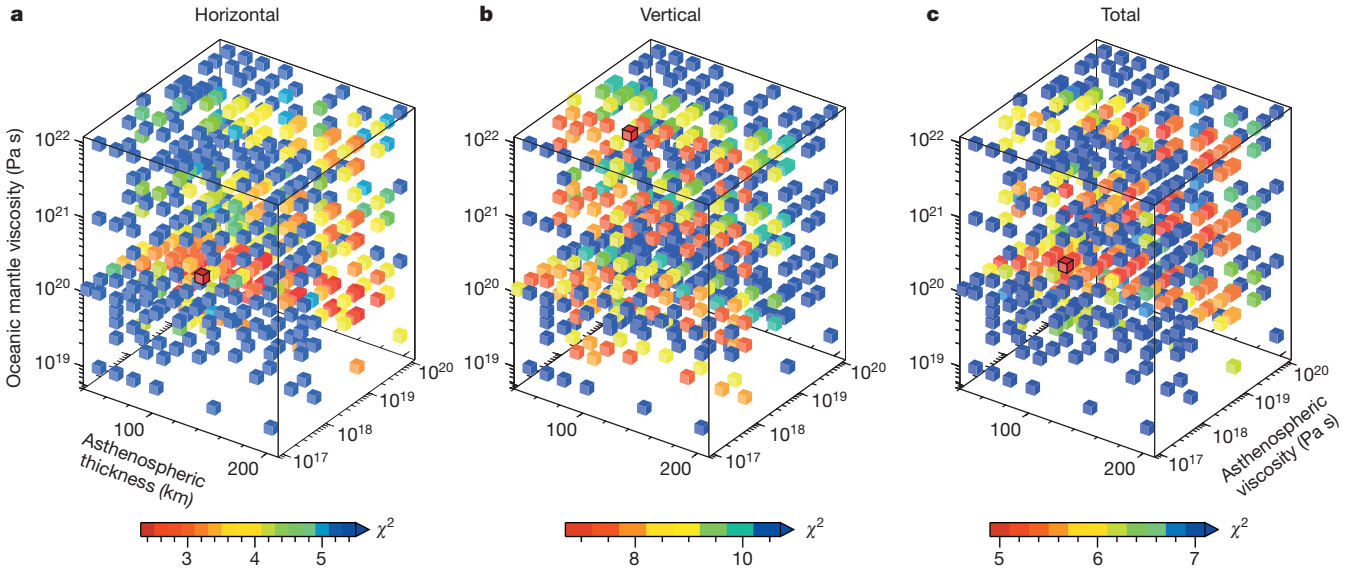

Figure 3 | Misfit of 652 test models considering variations in the asthenospheric thickness and viscosity, and oceanic mantle viscosity. Each cube represents one test model. Test models with red colour (low χ^2 values) reproduce the overall pattern of GNSS observations. The black-outlined cube represents the model with the lowest χ^2 value in each scenario. **a**, The χ^2 misfit is calculated from horizontal components. **b**, The χ^2 misfit is calculated from the vertical components. **c**, The χ^2 misfit is calculated from both horizontal and vertical components.

Their higher power of D_A may be due to the low spatial resolution of the GRACE data and the much greater lithospheric thickness and higher mantle viscosities of the North American interior. η_O is correlated with D_A and shows a modest anti-correlation with η_A (Fig. 4b, c).

The PM well reproduces the overall magnitude of the observed uplift in the midfield forearc area (Fig. 5a). The PM also reproduces the first-order pattern of the GNSS observations in the far field more than 500 km from the mainshock. The large misfit at stations between latitudes 0° and 6° S may be due to the low signal-to-noise ratio at those stations. The remaining misfits to the data, including the slight overestimates of the horizontal displacements in the mid-field, may indicate additional complexity of the rheology structure and other local processes, such as aftershocks and aseismic afterslip of the IOE, which are not considered in the PM. The PM predicted displacement evolution also matches the general curvature of the time series of the GNSS stations with three examples shown in Fig. 5b–d. The model predicts that the vertical displacement may soon reverse direction in the continental area, but not the horizontal components (Extended Data Fig. 10). The vertical component is more sensitive than the horizontal components to the change in the pattern of the viscoelastic flow above and beneath the slab caused by the existence of the elastic slab.

We did not include contributions from aseismic afterslip in the PM. We study the effects of stress-driven afterslip around the rupture segments of the IOE using the approach presented in Hu *et al.*[13], which relies on 2-km-thick low-viscosity tabular shear zones adjacent to the rupture. The afterslip model, regardless of assumed shear zone viscosity, overestimates the horizontal GNSS displacements (Extended Data Fig. 8a–d). Increasing the viscosity of the asthenosphere can lessen the effect of afterslip on the horizontal motions, but worsens the fit to the vertical GNSS component (Extended Data Fig. 8f). However, we cannot rule out a scenario of deep afterslip at depths of more than 50 km that produces displacements of up to 30 cm three years after the IOE in the near field but negligible motions at GNSS stations (Extended Data Fig. 8e). Nevertheless, substantial afterslip following the IOE, at

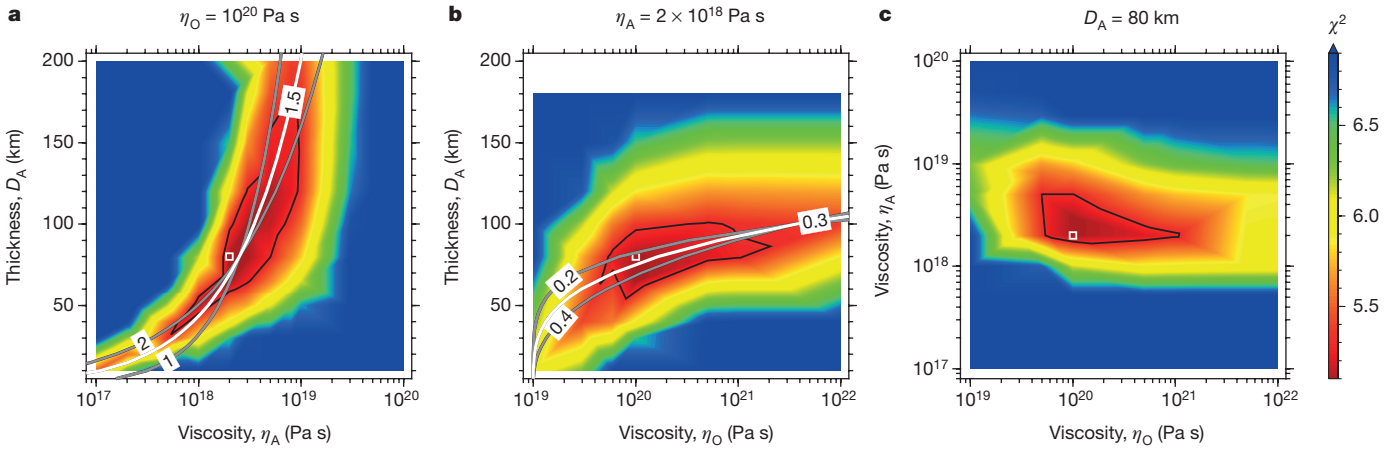

Figure 4 | Tradeoff between the viscosity of the oceanic upper mantle (η_O), the thickness (D_A) of the asthenosphere and its viscosity (η_A). The χ^2 misfit of the models is shown by the colour contours. Solid black lines represent the upper bound of $\chi^2 = 5.3$, below which the models match the overall pattern of the GNSS observations. White squares represent the PM. **a**, η_O is fixed at 10^{20} Pa s. The thick white line represents the preferred thickness–viscosity tradeoff relationship (with power 1.5): that is, $\eta_A = 3.5 \times 10^{15} D_A^{1.5}$. Grey lines represent different powers (1 and 2) of D_A. **b**, η_A is fixed at 2×10^{18} Pa s. The thick white line represents the preferred D_A–η_O relationship (with power 0.3): that is, $D_A = 75(\log_{10}\eta_O - 19)^{0.3}$. Grey lines represent different powers (0.2 and 0.4). **c**, D_A is fixed at 80 km.

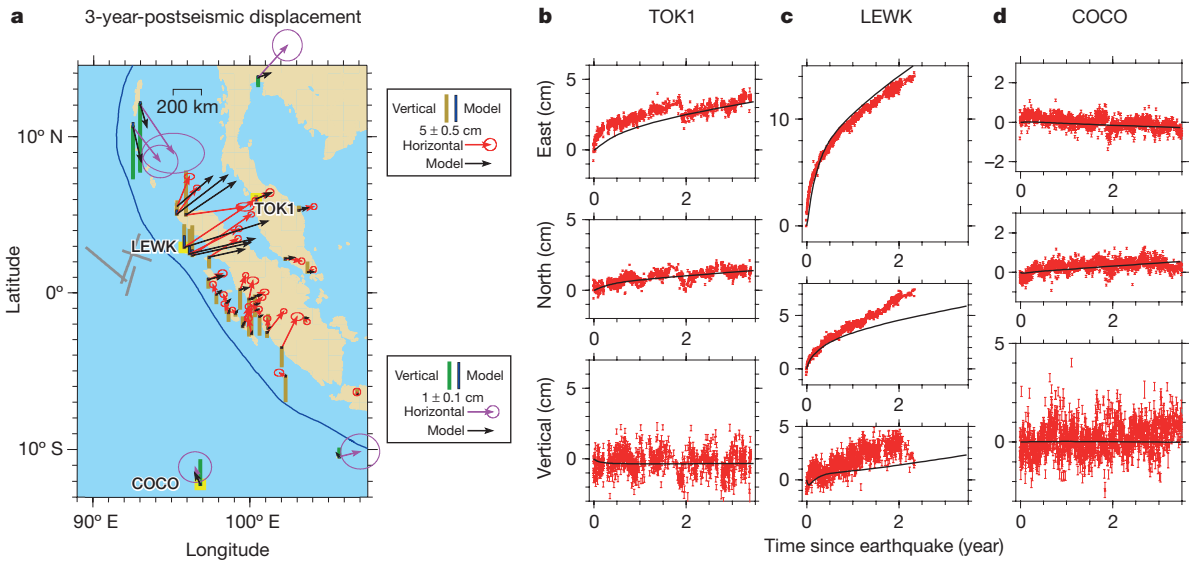

Figure 5 | Comparison of GNSS observations with predictions of the PM. a, Cumulative three-year-postseismic displacements. Red and magenta arrows represent observed horizontal GNSS displacements at different scales. Solid green and brown bars represent vertical GNSS observations at different scales. Black arrows and solid blue bars (note that for far-field stations, these are too small to be visible) represent horizontal and vertical model predictions, respectively. Yellow squares represent the locations of three example GNSS stations whose time series are shown in **b**–**d**. Thick grey lines represent the rupture segments of the IOE[6]. **b**–**d**, Comparison of GNSS time series with model-predicted displacements at stations TOK1, LEWK and COCO, respectively. Red dots with error bars indicating the 1σ uncertainties represent the GNSS observations. Black lines show model-predicted displacements.

shallow depths in particular, is unlikely to have occurred, as it would have produced subsidence in the northern Sumatra forearc.

If the asthenospheric layer terminates at the trench, this layer must have a lower viscosity or larger thickness to produce a comparable goodness of fit to the land GNSS data (Extended Data Fig. 9a, b). In the PM the oceanic asthenosphere extends with the subducting slab, based on some seismic imaging studies[17,19,20] and geodynamic modelling[21]. A denser geodetic network, particularly with near-field seafloor geodetic measurements, and a longer timespan of postseismic observations would help resolve this model ambiguity.

The purpose of this work is to study the first-order approximation of the viscoelastic relaxation of the upper mantle on the postseismic deformation of the 2012 earthquake. Therefore we do not consider a more complex thermal- and pressure-dependent rheology that may better represent the real Earth. Poroelastic rebound in the top layer of the lithosphere caused by the earthquake contributes to the postseismic deformation mainly in the vicinity of the rupture region[9], and is not considered in this work, which studies only the mid- and far-field deformation.

Improved knowledge of the depth and nature of the oceanic lithosphere–asthenosphere boundary and the rheology of the asthenosphere is essential to understanding the interplay of mantle convection and plate tectonics[22–24]. A weak asthenosphere lubricates plate tectonics, allows for rapid changes in plate motion, and enables lateral flow of upper-mantle material that produces vertical motions of the seafloor and continental margins[22,25]. A low-viscosity layer may also promote postseismic strain and stress transients that may affect seismicity rates over long distances and time spans[26]. A range of seismological and electrical resistivity observations show a sharp change in mantle properties at the boundary, indicating the presence of partial melt or water in the asthenosphere[27,28]. For example, Naif *et al.*[29] analysed sea-floor magnetotelluric data to reveal a partially melted channel less than 30 km thick along the lithosphere–asthenosphere boundary beneath the oceanic lithosphere of the Cocos plate. Stern *et al.*[30] relied on seismic reflection data to document a similar layer of approximately 10 km thickness at the base of the Pacific plate, subducting beneath the North Island of New Zealand. Other seismologic and petrological observations also favour a sharp boundary over a relatively thin, partially melted low-velocity zone[31–33] that decouples the oceanic lithosphere from the underlying mantle. Although there is a tradeoff between the viscosity and thickness of the low-viscosity layer on the lithosphere of the Indian Ocean, our results confirm the interpretation of the geophysical observations as reflecting the existence of a low-viscosity asthenosphere underlying the oceanic lithosphere.

Online Content Methods, along with any additional Extended Data display items and Source Data, are available in the online version of the paper; references unique to these sections appear only in the online paper.

Received 12 April; accepted 16 August 2016.
Published online 10 October 2016.

1. Wang, K., Hu, Y. & He, J. Deformation cycles of subduction earthquakes in a viscoelastic Earth. *Nature* **484,** 327–332 (2012).
2. Hu, Y., Wang, K., He, J., Klotz, J. & Khazaradze, G. Three-dimensional viscoelastic finite element model for post-seismic deformation of the great 1960 Chile earthquake. *J. Geophys. Res.* **109,** B12403 (2004).
3. Suito, H. & Freymueller, J. T. A viscoelastic and afterslip postseismic deformation model for the 1964 Alaska earthquake. *J. Geophys. Res.* **114,** B11404 (2009).
4. Meng, L. *et al.* Earthquake in a maze: compressional rupture branching during the 2012 M_w 8.6 Sumatra earthquake. *Science* **337,** 724–726 (2012).
5. Pollitz, F. F., Stein, R. S., Sevilgen, V. & Bürgmann, R. The 11 April 2012 east Indian Ocean earthquake triggered large aftershocks worldwide. *Nature* **490,** 250–253 (2012).
6. Wei, S., Helmberger, D. & Avouac, J.-P. Modeling the 2012 Wharton basin earthquakes off-Sumatra: complete lithospheric failure. *J. Geophys. Res. Solid Earth* **118,** 3592–3609 (2013).
7. Hill, E. M. *et al.* The 2012 M_w 8.6 Wharton Basin sequence: a cascade of great earthquakes generated by near-orthogonal, young, oceanic mantle faults. *J. Geophys. Res. Solid Earth* **120,** 3723–3747 (2015).
8. Feng, L. *et al.* A unified GPS-based earthquake catalog for the Sumatran plate boundary between 2002 and 2013. *J. Geophys. Res. Solid Earth* **120,** 3566–3598 (2015).
9. Hu, Y. *et al.* Contributions of poroelastic rebound and a weak volcanic arc to the postseismic deformation of the 2011 Tohoku earthquake. *Earth Planet Space* **66,** 106 (2014).
10. Han, S.-C., Sauber, J. & Pollitz, F. Coseismic compression/dilatation and viscoelastic uplift/subsidence following the 2012 Indian Ocean earthquakes quantified from satellite gravity observations. *Geophys. Res. Lett.* **42,** 3764–3772 (2015).
11. Pollitz, F. F., Banerjee, P., Grijalva, K., Nagarajan, B. & Bürgmann, R. B. Effect of 3-D viscoelastic structure on post-seismic relaxation from the 2004 M = 9.2 Sumatra earthquake. *Geophys. J. Int.* **173,** 189–204 (2008).

12. Wiseman, K., Bürgmann, R., Freed, A. M. & Banerjee, P. Viscoelastic relaxation in a heterogeneous Earth following the 2004 Sumatra-Andaman earthquake. *Earth Planet. Sci. Lett.* **431,** 308–317 (2015).
13. Hu, Y. *et al.* Stress-driven relaxation of heterogeneous upper mantle and time-dependent afterslip following the 2011 Tohoku earthquake. *J. Geophys. Res. Solid Earth* **121,** 385–411 (2016).
14. Sun, T. *et al.* Prevalence of viscoelastic relaxation after the 2011 Tohoku-Oki earthquake. *Nature* **514,** 84–87 (2014).
15. Bürgmann, R. & Dresen, G. Rheology of the lower crust and upper mantle: evidence from rock mechanics, geodesy, and field observations. *Annu. Rev. Earth Planet. Sci.* **36,** 531–567 (2008).
16. Yadav, R. K., *et al.* Coseismic offsets due to the 11 April 2012 Indian Ocean earthquakes (Mw 8.6 and 8.2) derived from GPS measurements. *Geophys. Res. Lett.* **40,** 3389–3393 (2013).
17. Shapiro, N. M., Ritzwoller, M. H. & Engdahl, E. R. Structural context of the great Sumatra-Andaman Islands earthquake. *Geophys. Res. Lett.* **35,** L05301 (2008).
18. Paulson, A. & Richards, M. A. On the resolution of radial viscosity structure in modelling long-wavelength postglacial rebound data. *Geophys. J. Int.* **179**(3), 1516–1526 (2009).
19. Song, T.-R. A. & Kawakatsu, H. Subduction of oceanic asthenosphere: evidence from sub-slab seismic anisotropy. *Geophys. Res. Lett.* **39,** L17301 (2012).
20. Huang, J. & Zhao, D. High-resolution mantle tomography of China and surrounding regions. *J. Geophys. Res.* **111,** B09305 (2006).
21. Liu, L. & Zhou, Q. Deep recycling of oceanic asthenosphere material during subduction. *Geophys. Res. Lett.* **42,** 2204–2211 (2015).
22. Bercovici, D., Tackley, P. & Ricard, Y. in *Treatise on Geophysics* Vol. 7 *Mantle Dynamics* (eds Bercovici, D. & Schubert, G.) 271–318 (Elsevier, 2015).
23. Weismüller, J. *et al.* Fast asthenosphere motion in high-resolution global mantle flow models. *Geophys. Res. Lett.* **42,** 7429–7435 (2015).
24. Höink, T., A. Jellinek, M. & Lenardic, A. Viscous coupling at the lithosphere–asthenosphere boundary. *Geochem. Geophys. Geosyst.* **12,** Q0AK02 (2011).
25. Colli, L. I. *et al.* Rapid South Atlantic spreading changes and coeval vertical motion in surrounding continents: evidence for temporal changes of pressure-driven upper mantle flow. *Tectonics* **32,** 1304–1321 (2014).
26. Pollitz, F. F., Bürgmann, R. & Romanowicz, B. Viscosity of oceanic asthenosphere inferred from remote triggering of earthquakes. *Science* **280,** 1245–1249 (1998).
27. Fischer, K. M., Ford, H. A., Abt, D. L. & Rychert, C. A. The lithosphere–asthenosphere boundary. *Annu. Rev. Earth Planet. Sci.* **38,** 551–575 (2010).
28. Karato, S. On the origin of the asthenosphere. *Earth Planet. Sci. Lett.* **321–322,** 95–103 (2012).
29. Naif, S., Key, K., Constable, S. & Evans, R. L. Melt-rich channel observed at the lithosphere–asthenosphere boundary. *Nature* **495,** 356–359 (2013).
30. Stern, T. A. *et al.* A seismic reflection image for the base of a tectonic plate. *Nature* **518,** 85–88 (2015).
31. Schmerr, N. The Gutenberg discontinuity: melt at the lithosphere-asthenosphere boundary. *Science* **335,** 1480–1483 (2012).
32. Yamamoto, J., Korenaga, J., Hirano, N. & Kagi, H. Melt-rich lithosphere–asthenosphere boundary inferred from petit-spot volcanoes. *Geology* **42,** 967–970 (2014).
33. Kawakatsu, H. *et al.* Seismic evidence for sharp lithosphere–asthenosphere boundaries of oceanic plates. *Science* **324,** 499–502 (2009).

Supplementary Information is available in the online version of the paper.

Acknowledgements This work was supported in part by HPC resources from the Arctic Region Supercomputing Center and the University of Alaska Fairbanks. J. He of the Geological Survey of Canada wrote the finite-element computer code used in this work. This work was funded by NSF award EAR-1246850 and benefited from support by the Miller Institute for Basic Research in Science to R.B. and a Singapore National Research Foundation Fellowship to E.M.H. (NRF-NRFF2010-064). J. Paul from the University of Memphis provided GPS data from the Andaman Islands. SuGAr is jointly maintained by the Earth Observatory of Singapore and the Indonesian Institute of Sciences (LIPI). This is Berkeley Seismological Laboratory contribution 2016-5.

Author Contributions Y.H. and R.B. together designed the study and did most of the writing. Y.H. carried out the numerical modelling. P.B., L.F. and E.M.H. collected and processed the daily time series of the SuGAr network. T.I. and T.T. collected and processed the daily time series of the AGNeSS network. K.W. assisted with the modelling strategy. All authors contributed to the interpretations and preparation of the final manuscript.

Author Information Reprints and permissions information is available at www.nature.com/reprints. The authors declare no competing financial interests. Readers are welcome to comment on the online version of the paper. Correspondence and requests for materials should be addressed to Y.H. (yhu@seismo.berkeley.edu).

Reviewer Information *Nature* thanks G. Hirth and W. Thatcher for their contribution to the peer review of this work.

METHODS

GNSS data. We collected and processed GNSS time series of 31 SuGAr and 2 AGNeSS stations following the strategy described in Feng *et al.*[8] using the GPS-Inferred Positioning System and Orbit Analysis Simulation Software (GIPSY-OASIS) version 6.2. GNSS daily time series of 11 IGS stations and 3 Memphis stations were downloaded from the Nevada Geodetic Laboratory (Nevada Bureau of Mines and Geology, University of Nevada; http://geodesy.unr.edu/index.php, last accessed on 28 July 2015). GNSS daily time series are processed in ITRF2008[34].

Over the past two decades a number of large subduction zone earthquakes occurred in Sumatra, including 17 events of moment magnitude $M_w \geq 6.5$ from 2009 up to the IOE (Extended Data Fig. 1). Based on the approach in ref. 9, we take the following steps to derive postseismic displacements from GNSS time series (Extended Data Figs 2 and 3). (1) We correct the time series for the trends of the postseismic transients of the earthquakes before the IOE. We fit the postseismic trends of the previous earthquakes with a logarithmic function of time. (2) We then calculate the long-term secular, annual and semi-annual variations of the time series before the IOE. (3) We correct the post-IOE time series for the trends obtained in step (2). (4) We fit the corrected post-IOE time series using logarithmic and exponential functions of time $a\log(1+t/\tau_{\log}) + b(1-\exp(-t/\tau_{\exp}))$, where a and b are constants, t is the time, and $\tau_{\log}$ and $\tau_{\exp}$ are characteristic time constants of the logarithmic and exponential terms, respectively. $\tau_{\log}$ and $\tau_{\exp}$ are determined for each GNSS station through a grid search method[9]. (5) We then calculate postseismic displacements between any two time epochs from the fitted postseismic curve (Extended Data Fig. 3). For those stations that were discontinued two or more years after the IOE we calculate the 3-year-postseismic displacements through the extended fitted curve.

We exclude the following ten stations that have data gaps or show patterns of postseismic displacements obviously inconsistent with that of their neighbouring stations (Extended Data Fig. 1). (1) CARI, AITB and NIMT have data gaps of more than 10 days before and after the IOE, 28 January to 23 April 2012, 2–26 April 2012 and 14 March to 26 April 2012, respectively. (2) NGNG and SLBU move westward almost perpendicular to the northward motion of neighbouring stations. PRKB moves southward, opposite to its neighbouring stations. (3) Horizontal displacements at PTLO, TLLU and KTET are more than five times larger than that of neighbouring stations within 100 km. The vertical displacement at BSAT is more than ten times larger than that of nearby stations. The inconsistency in the postseismic deformation pattern of the above stations is probably due to local processes and/or the bias in removing the postseismic trends of local earthquakes before the IOE. The signal-to-noise ratio at the two AGNeSS stations TANG and ACEH increased after 2014 owing to local construction activities. Since our postseismic displacements for TANG and ACEH are calculated through curve fitting based mostly on the time series of 2012–2014, we do not exclude these two AGNeSS stations.

We evaluate test models through calculating the weighted χ^2 misfit:

$$\chi^2 = \frac{1}{N-1-\text{d.o.f.}} \sum_{i=1}^{N} \frac{(G_i - F_i)^2}{\sigma_i^2} \quad (1)$$

where G and F represent GNSS displacement measurements and model predictions, respectively, i represents the station number, the degrees of freedom d.o.f. = 3 in this work are for the three free model parameters, σ_i^2 is the variance of the GNSS observation, and N is the total number of GNSS observations. We use six equally spaced time steps (that is, intervals of 6 months) covering the first three years after the IOE. We calculate the χ^2 misfit of the horizontal and vertical components separately. A linear sum of horizontal and vertical displacements produces preferred models that fit the horizontal components well, but provide a poor fit to the vertical component. Using a higher weight (such as 10) on the vertical component worsens the fit to horizontal components. Therefore we calculate the total effect by a combination of the horizontal components and five times the vertical component.

Finite-element model. The spherical-Earth viscoelastic finite-element model used in this work is based on previous studies of the Chile, Sumatra[12,13,35,36], and Cascadia subduction zones[1] and has been reported in refs 13 and 14. The model includes an elastic upper plate, an elastic slab, a viscoelastic mantle wedge, a viscoelastic oceanic asthenosphere and upper mantle (Fig. 2). Cooling and plate models[37–39] allow for a lithosphere thickness of 50–80 km of the 50–60-million-year-old Indian Ocean plate near the IOE. We thus assume a uniform lithospheric thickness of 50 km, which is also consistent with shear-wave tomography constraints[19] and the depth extent of the coseismic rupture of the IOE[6,7]. The shear moduli of the elastic lithosphere and viscoelastic upper mantle are assumed to be 48 GPa and 64 GPa, respectively. The Poisson's ratio and rock density are assumed to be 0.25 and 3.3×10^3 kg m^{-3}, respectively, for the entire domain. Viscoelastic relaxation of the upper mantle is represented by the bi-viscous Burgers rheology[15]. On the basis of previous studies[13] we assume the viscosity of the mantle wedge to be 3×10^{19} Pa s.

The coseismic fault slip of the earthquake derived by Wei *et al.*[6] is used in this work through the split-node method[40]. Different rupture models[6,7,16] do not change the fundamental pattern of the predicted co- and postseismic motions at GNSS stations hundreds of kilometres from the rupture area (Extended Data Fig. 4). Except for the top free surface, the other five model boundaries are free in the tangential directions and fixed in the normal direction. Domain boundaries are more than 1,000 km from the rupture zone in the horizontal directions. The bottom of the model is at 660 km depth, approximating the transition zone. The setup of the model boundaries produces negligible numerical artefacts on the deformation of the study area, containing these GNSS stations.

Model tests. We first present explorations of the model space, such as the lithospheric thickness, existence of the slab, and the extent of the oceanic asthenosphere. We examine the contribution of the relaxation in the individual rheological units to the surface deformation. Then we evaluate the potential contributions of afterslip of the fault to the postseismic deformation at GNSS stations. We report the range in three model parameters, the thickness (D_A) and viscosity (η_A) of the oceanic asthenosphere, and the viscosity of the oceanic upper mantle (η_O). Finally we present the temporal change in the postseismic surface deformation in the PM. In the following tests we vary some model parameters and keep other model parameters the same as in the PM, that is, $D_A = 80$ km, $\eta_A = 2 \times 10^{18}$ Pa s, $\eta_O = 10^{20}$ Pa s, and the viscosity of the mantle wedge $\eta_M = 3 \times 10^{19}$ Pa s (Fig. 2). We present model-predicted postseismic displacements at three years after the IOE. Differential surface deformation is calculated by the results of a test model minus that of the PM.

Exploration of the model space. If the oceanic asthenosphere has the same viscosity as the underlying oceanic upper mantle, that is, if we consider models with a homogeneous oceanic upper mantle[12–14], a test model with a viscosity of 10^{20} Pa s in the oceanic upper mantle predicts only about half of the observed postseismic horizontal displacements and subsidence of about 2 cm in the forearc area, in the first three years (Extended Data Fig. 5a). Lowering the viscosity (for example, by one order of magnitude; see Extended Data Fig. 5b) improves the fit to the horizontal GNSS data. However, the test model still fails to predict the observed uplift in the forearc region. A weak oceanic asthenosphere is required to produce the observed uplift.

We test a number of model scenarios in which the oceanic asthenosphere is not allowed to extend along the subducting slab, models without a slab, and models with different lithosphere thicknesses. Varying the lithospheric thickness by a couple of tens of kilometres produces negligible changes in the surface deformation (Extended Data Fig. 6a and b). Without the existence of the slab the model predicts additional landward motion near the trench, seaward motion inland, and uplift in the upper plate (Extended Data Fig. 6c). If we assume that the oceanic asthenosphere terminates at the trench and does not extend to greater depths beneath the slab, the differential surface motions three years after the IOE are up to approximately 5 cm near the trench (Extended Data Fig. 6d).

We have constructed test models to study the individual contributions of the rheological units to the surface deformation. We allow viscoelastic relaxation only in one rheological unit using its PM parameter and assume the rest of the domain to be elastic. Although this approach ignores the effects of the viscoelastic flow of other rheological units, it helps to understand the first-order pattern of the deformation that is due to each specific relaxation process.

If we allow viscoelastic relaxation only in the oceanic asthenosphere (Extended Data Fig. 7a), the test model VEA produces horizontal displacements up to more than 50 cm three years after the earthquake. The VEA produces postseismic uplift of more than 7 cm in the northern Sumatra forearc region. If we allow viscoelastic relaxation only in the oceanic upper mantle (Extended Data Fig. 7b), the test model VEO produces up to about 3 cm of the horizontal displacements. The magnitude of the vertical motions in the VEO is smaller than in the VEA, and its direction is opposite to that of the VEA. If we allow viscoelastic relaxation only in the mantle wedge (Extended Data Fig. 7c), the test model VEM produces generally landward motion of less than 5 cm and subsidence of less than 2 cm in the forearc area. Tests on the sensitivity of the surface deformation to variations in the viscosity of the rheological units also indicate that the relaxation in the oceanic asthenosphere has a more important role in controlling the viscoelastic postseismic crustal deformation than that of the underlying upper mantle and the mantle wedge above the subducting slab (results not shown). Note that the IOE induces stresses mostly at shallow depths (for example, less than about 400 km). The PM shows that the three-year-postseismic displacements are up to approximately 2 cm at depths of 400 km, and are negligibly small (less than 1 cm) at greater depths (exceeding 500 km) (results not shown). Therefore, viscoelastic postseismic surface deformation is controlled mainly by relaxation processes in the shallow upper mantle.

We simulate the afterslip after the IOE using a weak shear zone approach[14]. In a 2-km-thick shear zone extending down to a depth of 65 km, the maximum depth of the rupture of the IOE[6], we assume that the locked region is shaped by the 5-m coseismic contour lines within which no afterslip is allowed. Steady-state viscosity η_S in areas outside the locked region is assumed to be 5×10^{17} Pa s (ref. 13). If we do not allow viscoelastic relaxation in the upper mantle (afterslip only), the test model AFS produces substantial horizontal displacements mainly in the vicinities of the rupture area (Extended Data Fig. 7d). The vertical deformation in the AFS is similar to that of the VEO, that is, it produces subsidence in the forearc where postseismic uplift has been observed. If we apply the same weak shear zone to study the IOE-induced afterslip of the megathrust, the resultant change in the surface deformation is no more than 0.4 cm in the three years after the IOE because the stresses on the megathrust induced by the IOE over 200 km away are negligibly small (results not shown).

If we add the contribution from viscoelastic relaxation in the upper mantle using the PM parameters, that is, the model includes the three processes in Extended Data Fig. 7a and c, this afterslip model of $\eta_S = 5 \times 10^{17}$ Pa s produces horizontal displacements at least 50% larger than that in the PM (Extended Data Fig. 8a). Test models with different viscosities in the shear zone produce similar overestimated horizontal GNSS motion (Extended Data Fig. 8b and c). Overestimated motions at GNSS sites are mostly due to afterslip at shallow depths ($\leq$50 km) (Extended Data Fig. 8d). Earthquake-induced stress at greater depths (>50 km) are much smaller, and thus the stress-driven deep afterslip slightly overestimates midfield motions and predicts little changes in the far field (Extended Data Fig. 8e). An afterslip model with a low $\eta_S = 5 \times 10^{17}$ Pa s and a higher η_A (such as $\eta_A = 10^{20}$ Pa s), two orders of magnitude higher than in the PM, produces a better fit to the horizontal GNSS data but worsens the fit to the vertical component (Extended Data Fig. 8f). As afterslip produces subsidence at the northern Sumatra stations, adding its contributions generally increases the model misfits.

In the PM the oceanic asthenosphere extends to greater depths with the downgoing slab. We constructed a test model in which the oceanic asthenospheric layer terminates at the trench[41]. Excluding the subducted asthenosphere results in subsidence of up to about 2 cm and southwest seaward displacements of up to about 5 cm in the forearc (Extended Data Fig. 6d). A much lower viscosity (such as $\eta_A = 2 \times 10^{17}$ Pa s; see Extended Data Fig. 9a) or larger thickness (such as $D_A = 200$ km; see Extended Data Fig. 9b) of the asthenosphere is then required to produce a comparable goodness of fit to the land GNSS data.

We assumed a sharp boundary between the lithosphere and the asthenospheric layer and did not include details of the lithosphere–asthenosphere boundary because of the limits of the spatial coverage of the GNSS network. We constructed a test model to study the effect of including a rheological transition between the lithosphere and asthenosphere. In the test model we assume a 20-km-thick transition zone in which the viscosity decreases linearly with depth from 10^{22} Pa s at the bottom of the lithosphere to the preferred 2×10^{18} Pa s of the asthenosphere. Other model parameters are the same as in the PM. This transition-zone model produces a change of no more than 5 cm in surface displacements in areas within 200 km of the rupture area and approximately zero at the land GNSS stations in the first three years after the IOE (Extended Data Fig. 9c). This test thus indicates that the sharpness of the lithosphere and asthenosphere boundary cannot be resolved by the sparse geodetic observations.

Overall the relaxation in the oceanic asthenosphere is the primary process controlling the postseismic surface deformation and is the only process that produces the observed uplift in the northern Sumatra forearc. Surface deformation is much more sensitive to the rheological structure below the oceanic lithosphere than to that on the continental side where most of the GNSS stations are located. These test models thus illustrate that the IOE provides a unique opportunity to constrain the rheological structure of the oceanic upper mantle.

Range in model parameters and future predictions in PM. We derive the range of the model parameters by selecting those test models fitting the overall pattern of the GNSS data in both horizontal and vertical directions. The test model best fitting the horizontal GNSS data has $\chi^2 = 5.8$ and does not predict the observed uplift in northwestern Sumatra forearc (Extended Data Fig. 9d). The test model best fitting the vertical GNSS data has $\chi^2 = 6.96$ and overestimates the horizontal data (Extended Data Fig. 9e). We have found that test models with $\chi^2 \leq 5.3$ reproduce the first-order pattern of the GNSS data, that is, misfit of the horizontal components is less than about 20%, and the model predicts more than about 20% of observed uplift at these closest GNSS stations, such as UMLH, LEWK, BNON and BSIM. Test models of $\chi^2 \leq 5.3$ in Fig. 3c thus give the ranges as $D_A = 30$–200 km, $\eta_A = (0.5$–$10) \times 10^{18}$ Pa s, and $\eta_O = (0.5$–$100) \times 10^{20}$ Pa s.

We examine the evolution of the spatial pattern of the predicted viscoelastic postseismic surface deformation in the PM following the IOE (Extended Data Figs 10). The peak horizontal displacements in the upper plate increase from around 10 cm one year after the IOE to more than 50 cm ten years after the IOE (Extended Data Figs 10a–c). Horizontal displacements increase steadily over time and exhibit only small changes in orientation (Extended Data Fig. 10d, e).The vertical surface displacements are generally divided into four uplift–subsidence quadrants, a common pattern of the postseismic deformation following a strike–slip earthquake. An interesting feature is the change in the direction of the vertical displacement in the northeastern quadrant in the continental upper plate (Extended Data Fig. 10a–c, f). In this quadrant the vertical motion one year after the IOE is uplift near the rupture area and subsidence farther inland (Extended Data Fig. 10a, f). The area of the subsidence region shrinks with time, and the uplift region expands.

34. Altamimi, Z., Collilieux, X. & Métivier, L. ITRF2008: An improved solution of the International Terrestrial Reference Frame. *J. Geodyn.* **85,** 457–473 (2011).
35. Hippchen, S. & Hyndman, R. D. Thermal and structural models of the Sumatra subduction zone: implications for the megathrust seismogenic zone. *J. Geophys. Res.* **113,** B12103 (2008).
36. Hu, Y. & Wang, K. Spherical-Earth finite element model of short-term postseismic deformation following the 2004 Sumatra earthquake. *J. Geophys. Res.* **117,** B05404 (2012).
37. Müller, R. D. *et al.* Digital isochrons of the world's ocean floor. *J. Geophys. Res.* **102,** 3211–3214 (1997).
38. Jacob, J., Dyment, J. & Yatheesh, V. Revisiting the structure, age, and evolution of the Wharton Basin to better understand subduction under Indonesia. *J. Geophys. Res. Solid Earth* **119,** 169–190 (2014).
39. Beghein, B., Yuan, Y., Schmerr, N. & Xing, Z. Changes in seismic anisotropy shed light on the nature of the Gutenberg discontinuity. *Science* **343,** 1237–1240 (2014).
40. Melosh, H. J. & Raefsky, A. A simple and efficient method for introducing faults into finite element computations. *Bull. Seismol. Soc. Am.* **71,** 1391–1400 (1981).
41. Hawley, W. B., Allen, R. M. & Richards, M. A. Tomography reveals buoyant asthenosphere accumulating beneath the Juan de Fuca plate. *Science.* **353,** 1406–1408 (2016).

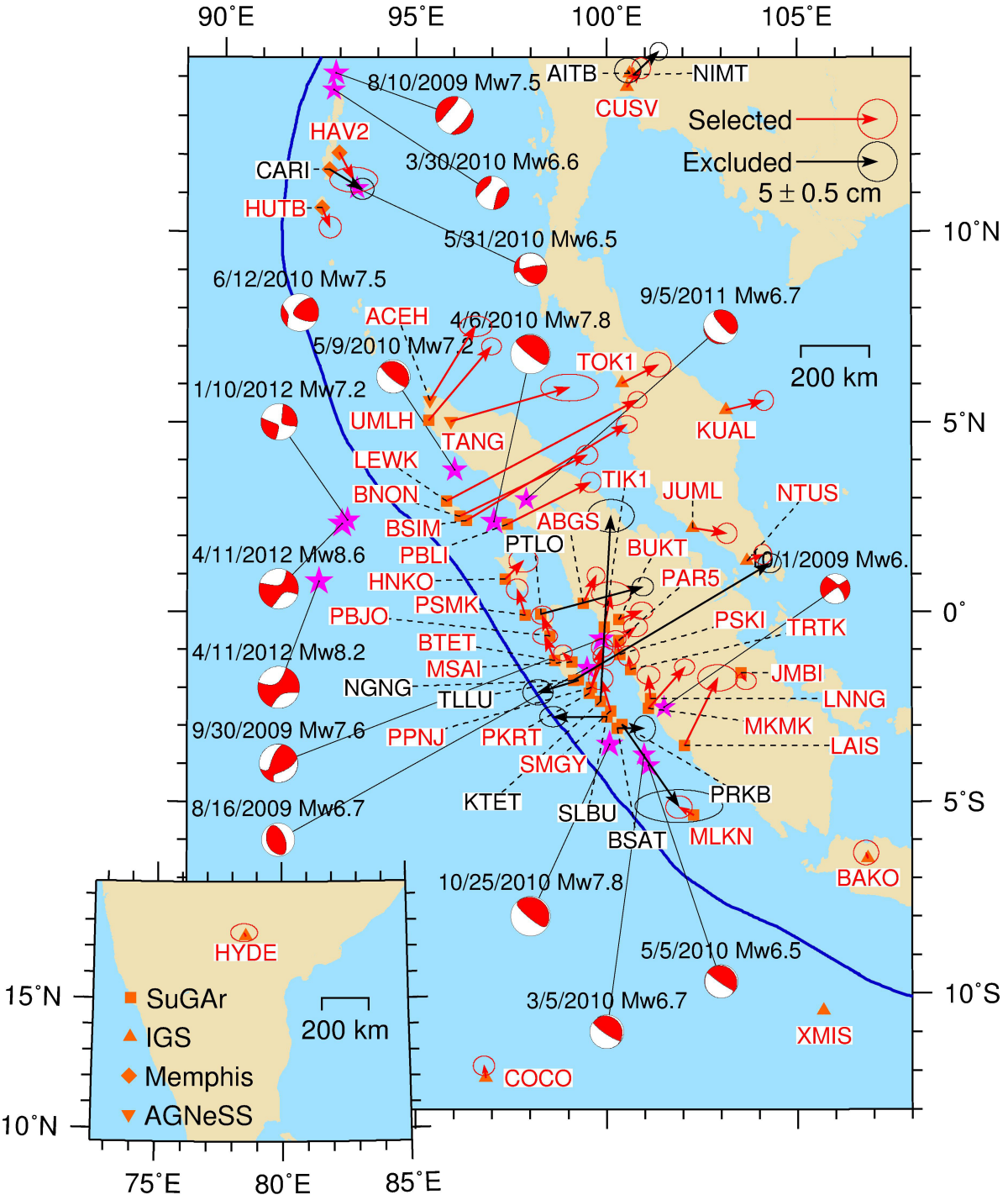

Extended Data Figure 1 | Location of GNSS stations and earthquakes of $M_w \geq 6.5$ from 2009 up to the IOE. Magenta stars represent epicentres of the pre-IOE earthquakes. Red and black arrows represent two-year-postseismic displacements at stations that are used or are excluded in this work, respectively. Station names are labelled with the same colour coding. Solid brown squares, triangles, diamonds and inverted triangles represent GNSS from the SuGAr, IGS, Memphis and AGNeSS networks, respectively.

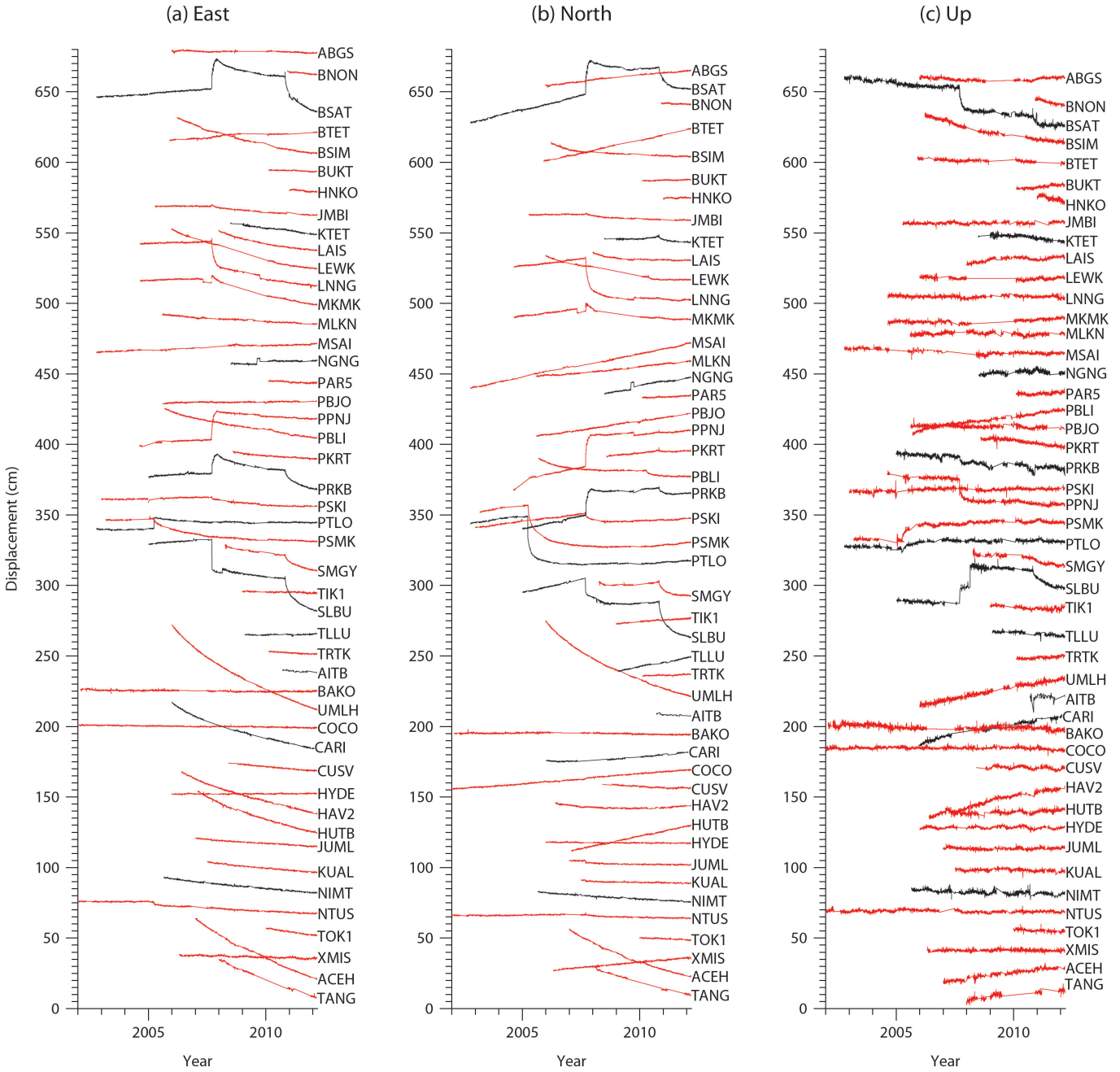

Extended Data Figure 2 | Pre-earthquake daily time series recorded at the GNSS stations shown in Extended Data Fig. 1. **a**, **b** and **c** show the east, north and up components of the time series, respectively. Coseismic static offsets of one day before and after the earthquakes shown in Extended Data Fig. 1 are removed from the time series. The time series include the total effects of postseismic deformation of previous earthquakes, secular deformation, annual and semi-annual variations. Red and black time series represent those stations that are selected or are excluded in this work, respectively, using the same colour coding as for the station names in Extended Data Fig. 1.

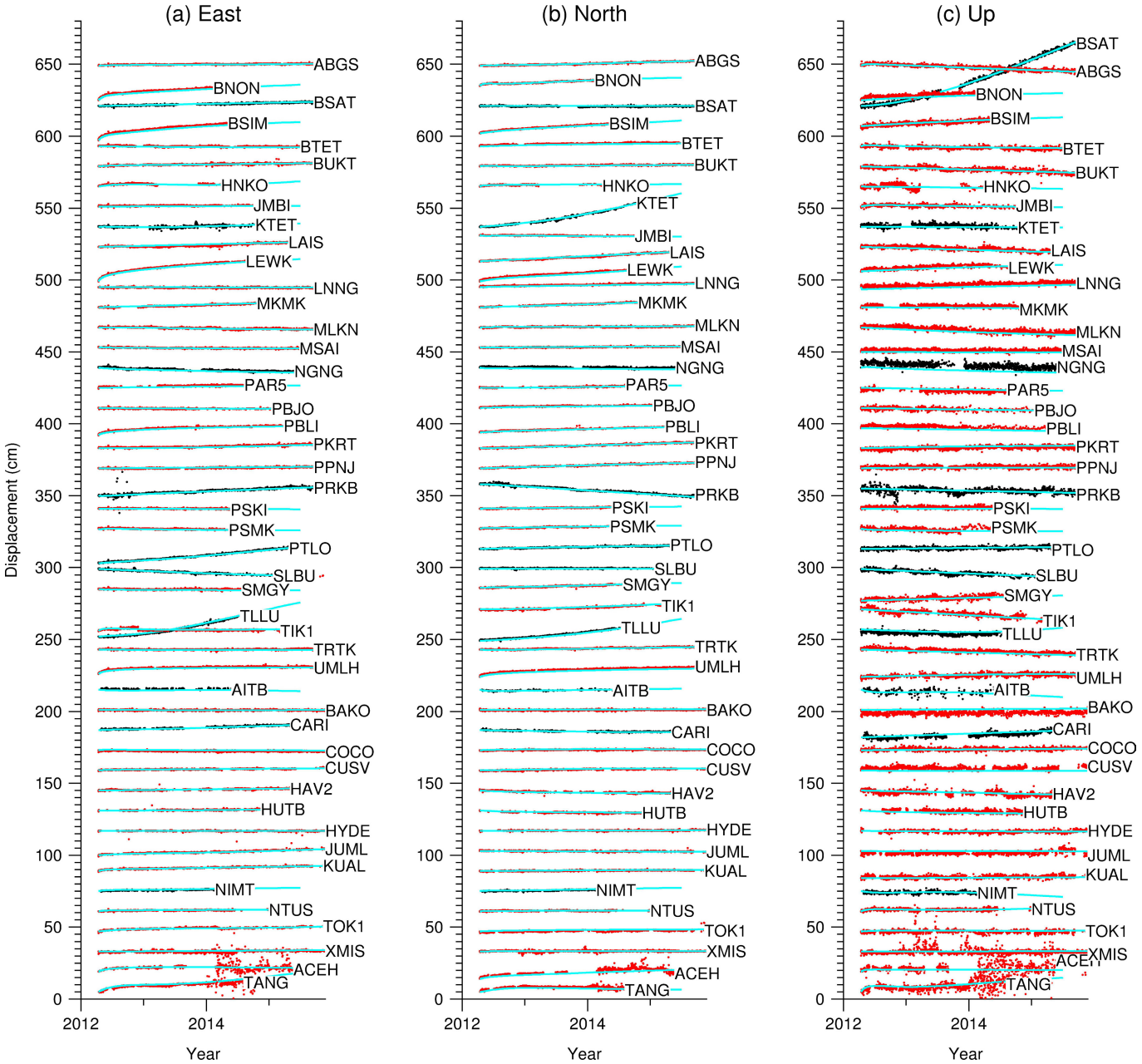

Extended Data Figure 3 | Postseismic GNSS time series after removing postseismic deformation of previous earthquakes, secular motion and seasonal variations. a, **b** and **c** show the east, north and up components of the time series, respectively. Red and black lines represent those stations that are selected or are excluded in this work, respectively. Continuous cyan curves fitted to the postseismic time series are used to constrain our postseismic deformation models.

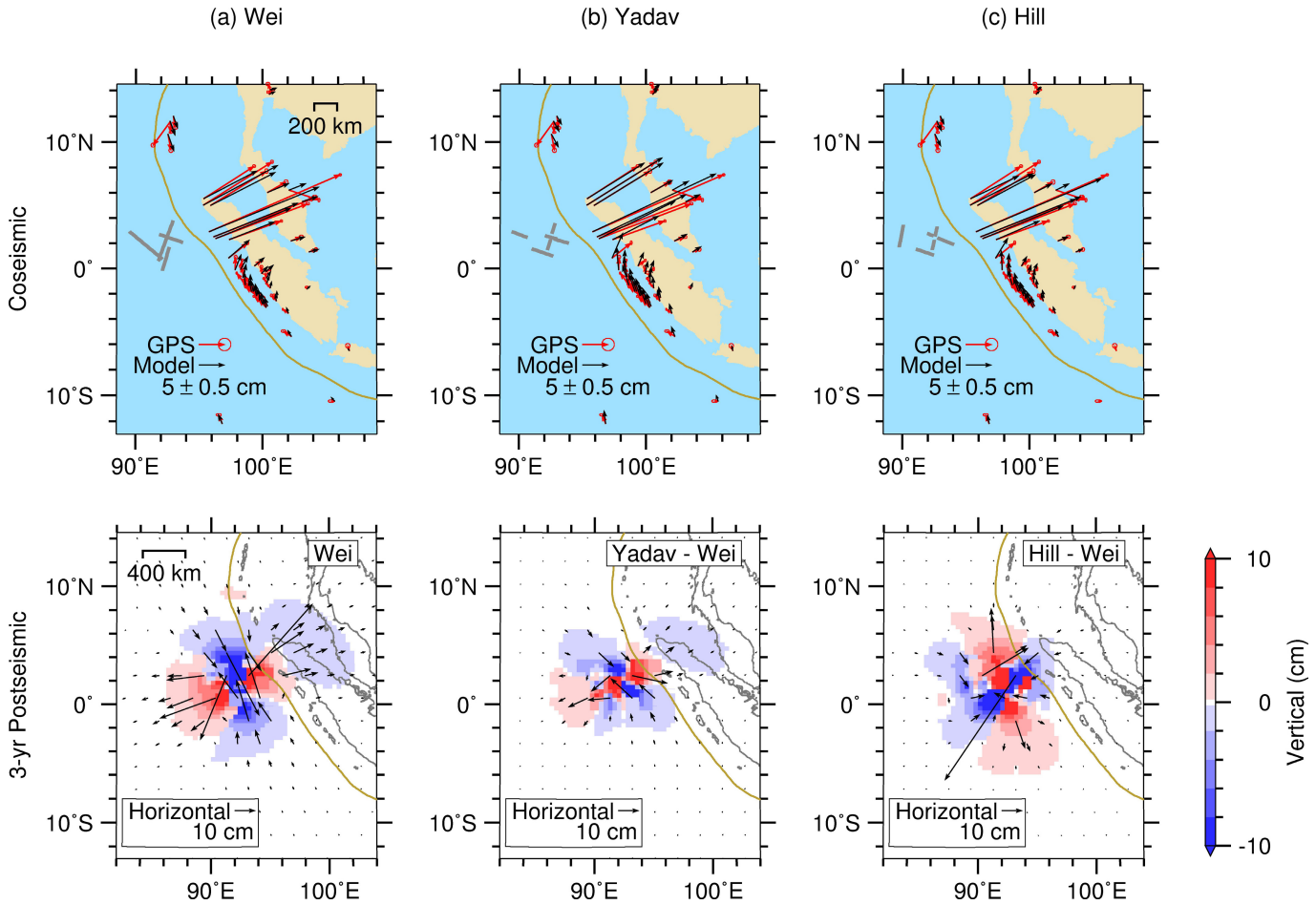

Extended Data Figure 4 | Comparison of different source models of the IOE. a, The coseismic slip distribution is from Wei *et al.*[6], who inverted regional and teleseismic waveform data. Their fault slip model was used in this work. Coseismic GNSS observations are estimated from static offsets of five days before and after the IOE. **b**, The coseismic slip distribution is from Yadav *et al.*[16], who inverted static offsets of 5 days before and after the IOE of daily GNSS data. Model predictions are scaled by 0.8 to fit the coseismic GNSS data better. **c**, The coseismic slip distribution is from Hill *et al.*[7], who inverted static offsets of about 10 min before and after the IOE of high-rate (one-second rate) GNSS data in the middle field and of 10 days before and after the IOE of daily GNSS data in the far field. Model predictions are scaled by 1.5 to fit the same GNSS data also shown in **a** and **b** better. In the upper panels red and black arrows represent coseismic GNSS observations and model-predicted displacements, respectively. Thick grey lines represent inverted rupture segments of the IOE. In the lower panel of **a** black arrows and colour contours represent model-predicted three-year-postseismic horizontal and vertical displacements, respectively. In the lower panels of **b** and **c** displacements are differenced by the test model minus the model in **a**.

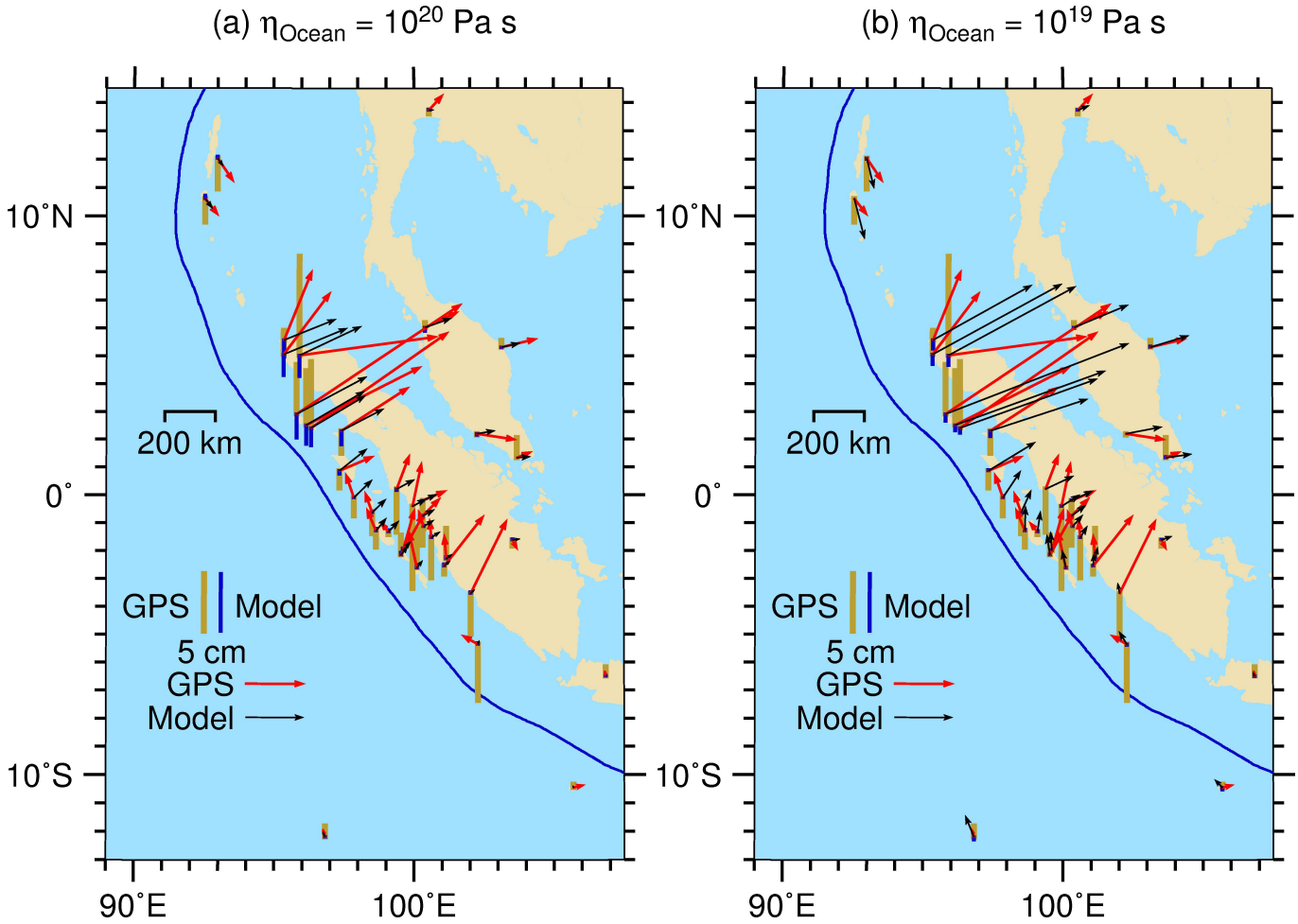

Extended Data Figure 5 | Comparison of three-year-postseismic GNSS observations with predicted displacements in test models of a homogeneous oceanic upper mantle below 50 km without the low-viscosity oceanic asthenosphere. Red and black arrows represent horizontal GNSS observations and horizontal model-predicted displacements, respectively. Solid brown and blue bars represent vertical GNSS observations and vertical model-predicted displacements, respectively. **a**, Viscosity of the oceanic upper mantle is 10^{20} Pa s. **b**, Viscosity of the oceanic upper mantle is 10^{19} Pa s.

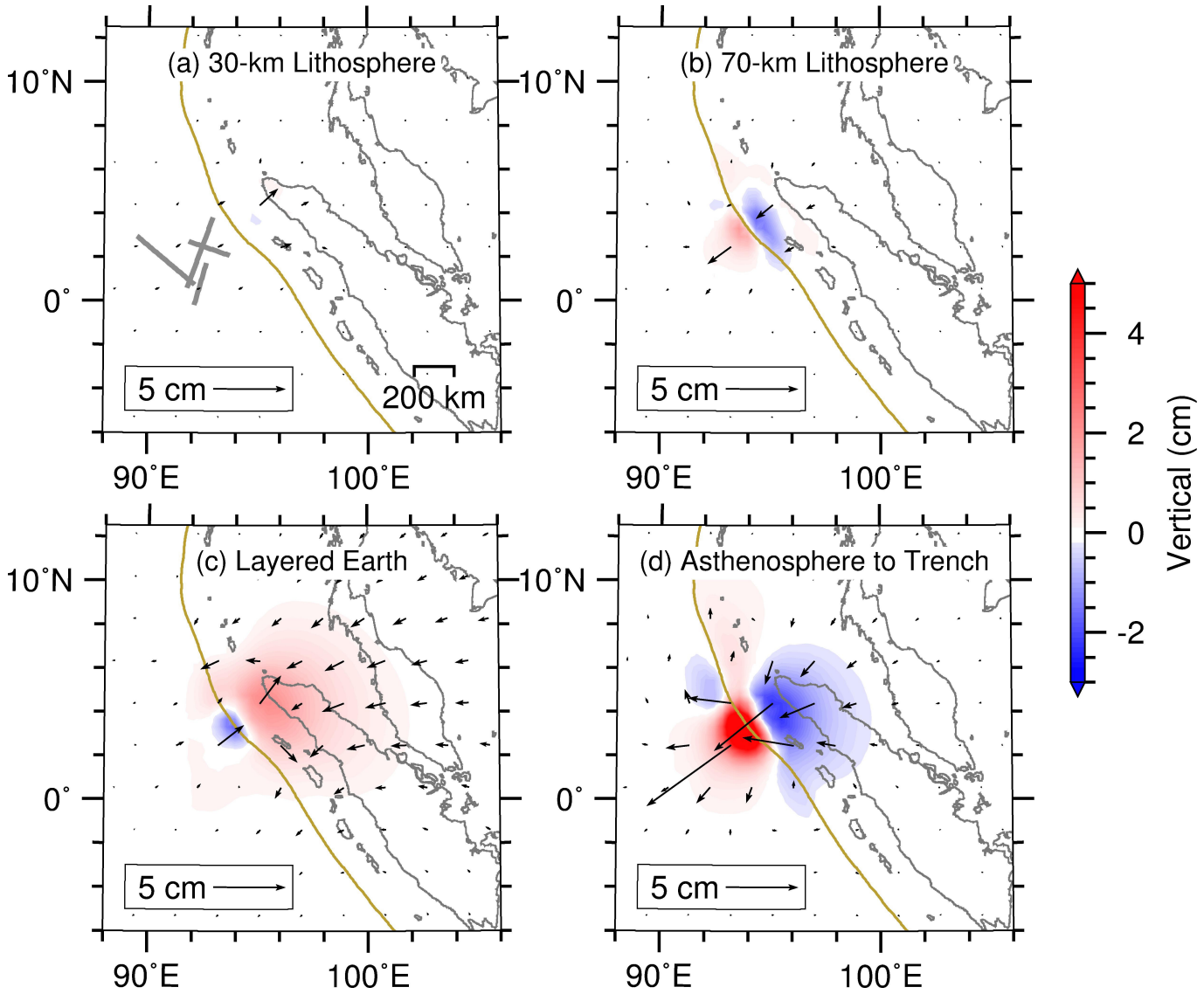

Extended Data Figure 6 | Effects of the extent of the oceanic asthenosphere, layered Earth and variation in the lithospheric thickness on the surface deformation. Displacements are differenced by a test model minus the PM in which the lithospheric thickness, the thickness (D_A) and viscosity (η_A) of the asthenospheric top layer, and the viscosity in the underlying oceanic upper mantle (η_O) are 50 km, 80 km and 2×10^{18} Pa s, and 10^{20} Pa s, respectively. Black and coloured contours represent the horizontal and vertical displacements, respectively. Thick brown lines outline the location of the trench. **a**, In the test model the lithospheric thickness is assumed to be 30 km, that is, 20 km thinner than in the PM. **b**, Similar to **a** except that the lithospheric thickness is 70 km. **c**, In the test model the slab does not exist. **d**, In the test model the oceanic asthenosphere terminates at the trench and does not extend with the downgoing subducting slab. Thick grey lines in **a** represent rupture segments of the IOE.

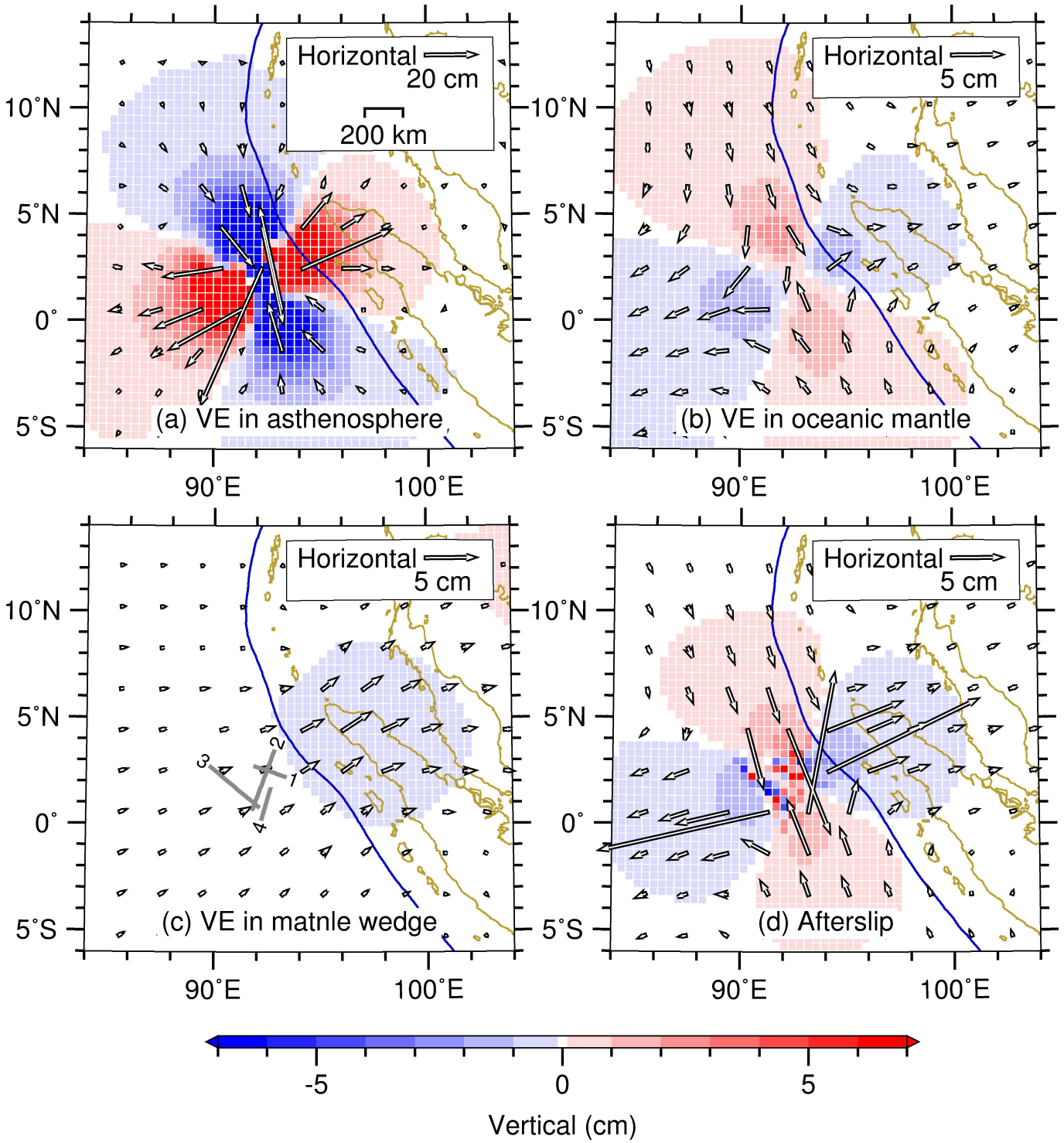

Extended Data Figure 7 | Contributions of viscoelastic relaxation in the rheological units and afterslip of the IOE to the cumulative three-year-postseismic surface deformation. **a**, Surface deformation due to viscoelastic relaxation in the oceanic asthenosphere alone. The continental and oceanic upper mantle are assumed to be elastic. **b**, Surface deformation due to viscoelastic relaxation in the oceanic upper mantle alone. **c**, Surface deformation due to viscoelastic relaxation in the mantle wedge alone. Thick grey lines represent the rupture segments of the IOE. **d**, Surface deformation due to the modelled afterslip in the shear zone assuming no viscoelastic relaxation elsewhere. Open arrows and colour contours represent horizontal and vertical model-predicted displacements, respectively.

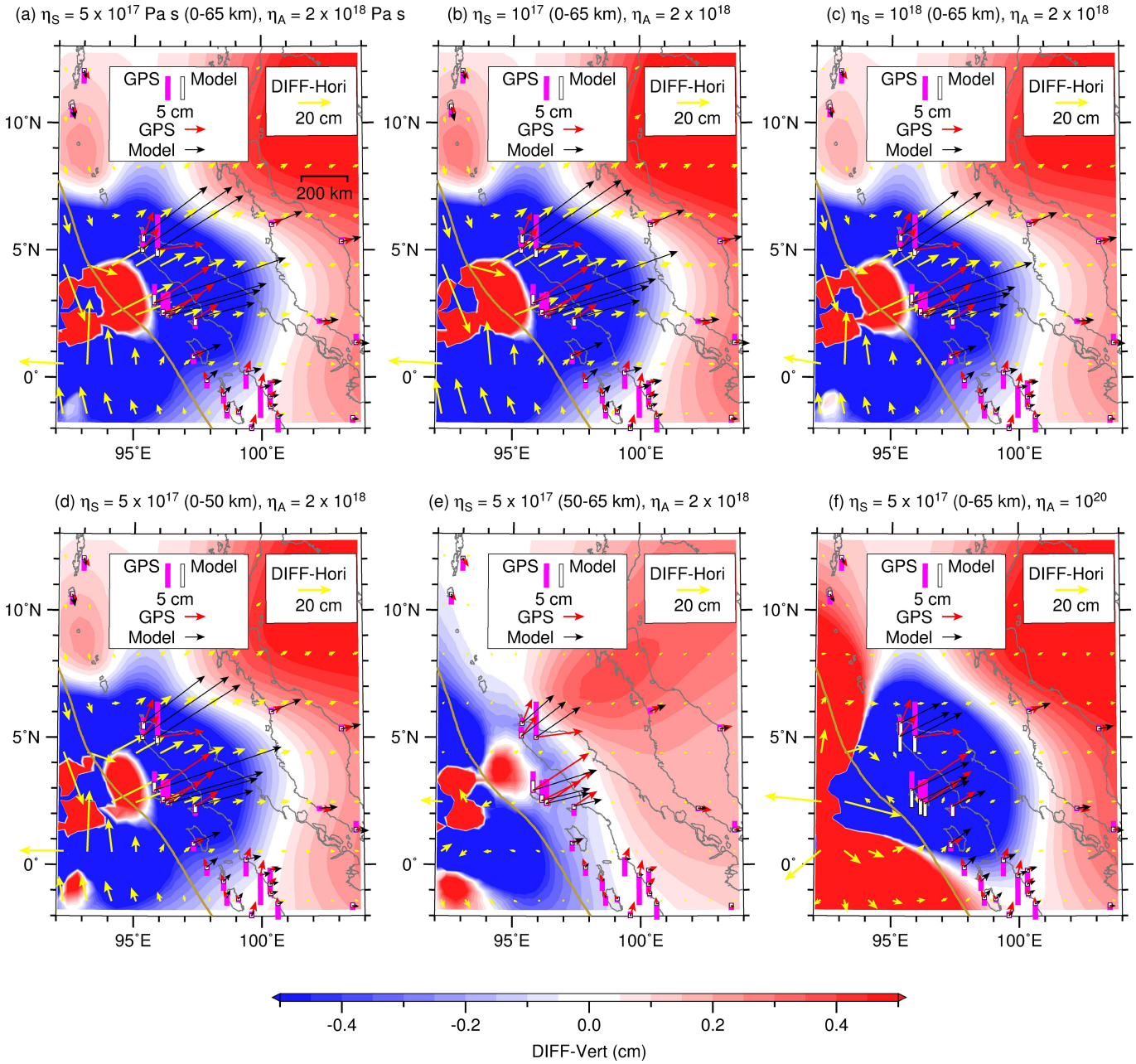

Extended Data Figure 8 | Effects of afterslip after the IOE on the surface deformation. a, Steady-state viscosity in the afterslip shear zone η_S is 5×10^{17} Pa s, and $\eta_A = 2 \times 10^{18}$ Pa s. Afterslip is allowed at depths 0–65 km. Red and black arrows represent horizontal GNSS observations and model-predicted displacements, respectively. Solid magenta and white bars represent vertical GNSS observations and model-predicted displacements, respectively. Yellow arrows and colour contours represent differential horizontal (DIFF − Hori) and vertical (DIFF − Vert) components by the test model minus the PM, respectively. **b**, Similar to **a** except with a low $\eta_S = 10^{17}$ Pa s. **c**, Similar to **a** except with a high $\eta_S = 10^{18}$ Pa s. **d**, Similar to **a** except that the afterslip is allowed only at shallow depths ($\leq$50 km) and no deep afterslip. **e**, Similar to **a** except that the afterslip is allowed only at greater depths (50–65 km), and no shallow afterslip. **f**, $\eta_S = 5 \times 10^{17}$ Pa s, and $\eta_A = 10^{20}$ Pa s. Afterslip is allowed at depths of 0–65 km.

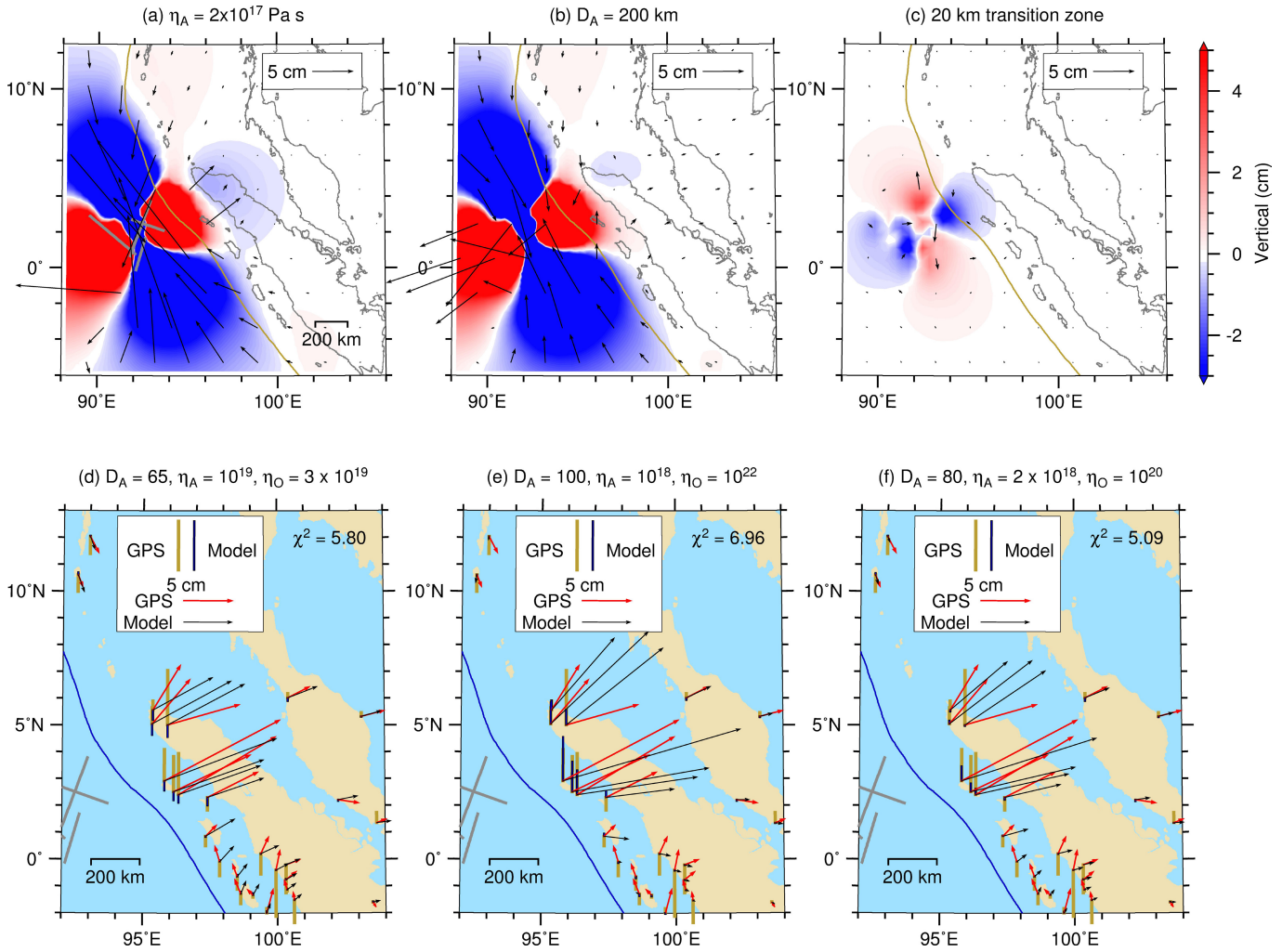

Extended Data Figure 9 | Three-year-postseismic displacements due to changes in model parameters and comparison of GNSS observations with predicted displacements. a, Surface deformation calculated by the test model minus the PM. In the test model the asthenosphere terminates at the trench and does not extend with the downgoing slab. η_A is one order of magnitude lower than that of the PM. Other model parameters are the same as the PM. Black arrows and contours represent horizontal and vertical three-year-postseismic surface displacements, respectively. Thick grey lines represent rupture segments of the IOE. **b**, Similar to **a** except that η_A is the same as in the PM but $D_A = 200$ km, more than two times thicker than that of the PM. **c**, The sharp boundary between the lithosphere and the asthenosphere in the PM is replaced by a 20-km-thick transition zone in which the viscosity decreases linearly with depth from 10^{22} Pa s at the bottom of the lithosphere to the preferred 2×10^{18} Pa s of the asthenosphere. **d** and **e** are the test models best fitting to the horizontal (Fig. 3a) and vertical (Fig. 3b) GNSS observations, respectively. Red and black arrows represent horizontal GNSS observations and horizontal model-predicted displacements, respectively. Solid brown and blue bars represent vertical GNSS observations and vertical model-predicted displacements, respectively. Thick grey lines represent the rupture segments of the IOE. **f**, Preferred lowest misfit test model (PM) best fitting to both horizontal and vertical GNSS data (Fig. 3c), the same data as in Fig. 5a. Values of the viscosity of the oceanic upper mantle (η_O), thickness (D_A) and viscosity (η_A) of the asthenosphere in each test model are labelled on the top of each plot in **d** and **e**. The value of χ^2 in each test model is labelled as inset text.

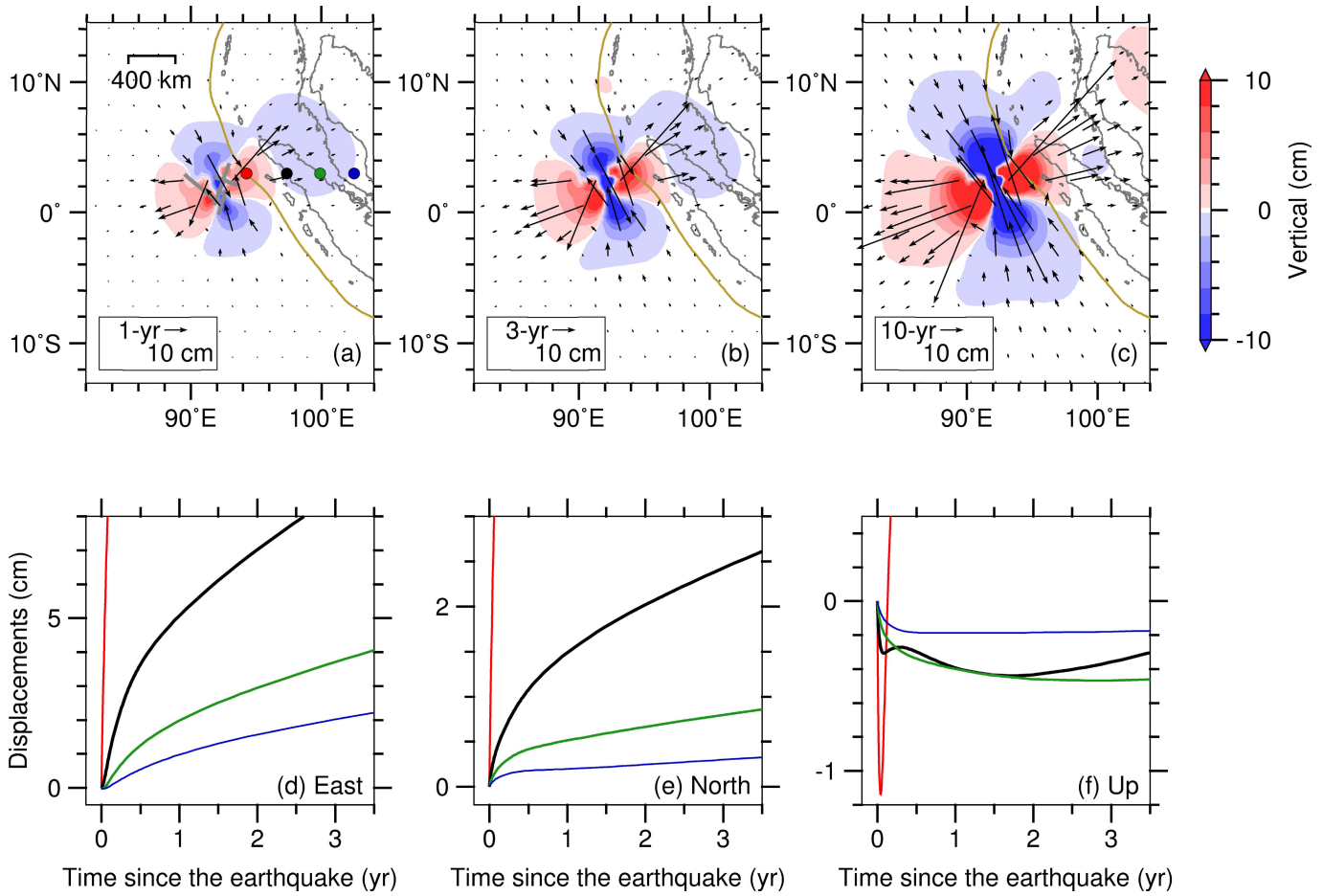

Extended Data Figure 10 | Postseismic displacement evolution in the PM. a, **b** and **c** show cumulative surface postseismic displacements at one year, three years, and ten years after the earthquake, respectively. Black arrows and contours represent horizontal and vertical displacements, respectively. Thick grey lines in **a** represent the rupture segments of the IOE. **d**, **e** and **f** show the evolution of postseismic displacements in the east, north and up directions, respectively, at four surface example points of the same latitude 3° N whose locations are at trench (red lines), western (black) and eastern (green) coast of Sumatra, and inland (blue). Locations of these four points are also shown as solid dots in **a** with the same colour coding.